Materials Advances

Accepted Manuscript

This article can be cited before page numbers have been issued, to do this please use: H. Sun, C. Tan, X. Tan, H. Wang, Y. Yin, Y. Song, G. Liu, J. G. Noudem, Q. Jiang, J. Zhang, H. Huang and J. Jiang, *Mater. Adv.*, 2020, DOI: 10.1039/D0MA00405G.

View Article Online
DOI: 10.1039/D0MA00405G

Table of Contents Entry

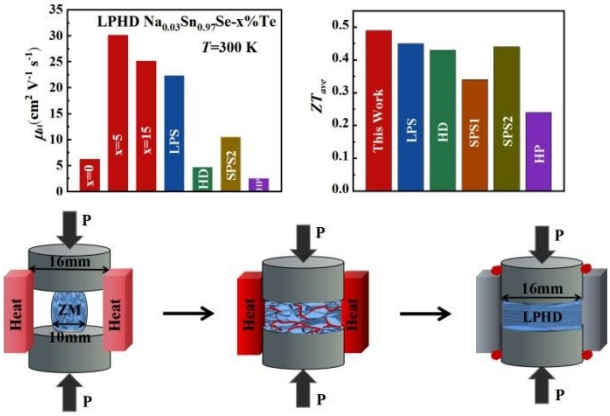

An unconventional liquid-phase hot deformation technique was used to prepare $Sn_{0.97}Na_{0.03}Se$ thermoelectric materials, leading to high orientation with good thermoelectric properties.

View Article Online
DOI: 10.1039/D0MA00405G

ARTICLE

Boosted carrier mobility and enhanced thermoelectric properties of polycrystalline $Na_{0.03}Sn_{0.97}Se$ by liquid-phase hot deformation

Received 00th January 20xx,
Accepted 00th January 20xx

DOI: 10.1039/x0xx00000x

Hao Sun,[a,b] Chang Tan,[b] Xiaojian Tan,[b,*] Hongxiang Wang,[b] Yinong Yin,[b] Yuexin Song,[a,b] Guo-Qiang Liu,[b] Jacques G. Noudem,[c] Quanguo Jiang,[a] Jianfeng Zhang,[a] Huajie Huang,[a,*] and Jun Jiang[b,*]

SnSe emerges as a promising thermoelectric material due to an ultrahigh *ZT* value in its single crystal while polycrystalline SnSe offers much lower *ZT*s resulting from the weak texturing degree. Here, we report a liquid-phase hot deformation technique to enhance the texturing degree of polycrystalline $Na_{0.03}Sn_{0.97}Se$, leading to a significantly boosted carrier mobility of 30.1 $cm^2 V^{-1} s^{-1}$ at room temperature and a remarkable average power factor of 5.73 μW $cm^{-1} K^{-2}$ between 300 and 830 K. Moreover, the liquid-phase hot deformation procedure introduces dense dislocation defects and realizes an obviously reduced lattice thermal conductivity of 0.40 W $m^{-1} K^{-1}$ at 747 K. Consequently, a peak *ZT* of 0.9 at 780 K and a high average ZT_{ave} of 0.49 from 300 to 830 K were obtained for the polycrystalline $Na_{0.03}Sn_{0.97}Se$ sample. This work presents that the liquid-phase hot deformation is a convenient and energy-saving strategy to enhance the texturing degree and improve the thermoelectric performance in polycrystalline SnSe materials.

1. Introduction

In the past few decades, thermoelectric (TE) materials have drawn great attention due to their capacity of direct conversion between heat and electricity.[1-5] The conversion efficiency of TE materials is quantified by the dimensionless figure of merit $ZT = \alpha^2\sigma T/\kappa$, where α is the Seebeck coefficient, σ is the electrical conductivity, κ is the thermal conductivity (including the carrier κ_e and lattice κ_l contributions), and T is the operating temperature. The excellent TE performance could be realized by increasing the power factor (PF = $\alpha^2\sigma$) or compressing the thermal conductivity as much as possible.[6-8] Usually, several strategies such as resonant doping,[9,10] band convergence[11-13] and carrier concentration optimization[14,15] can effectively increase the power factor, while the lattice thermal conductivity κ_l can be reduced by the all-scale hierarchical structuring[16-19] and dense defects[20-23] as phonon scattering centers.

As an emerging TE material, the earth-abundant and environmental-friendly binary compound tin selenide (SnSe) has attracted widespread attention owing to its intrinsic ultralow thermal conductivity[24-26] and record-high *ZT* values for both *p*-type (2.6 at 923 K)[27] and *n*-type (2.8 at 773 K)[28] SnSe single crystals. Although the SnSe single crystals exhibit high *ZT*s, the poor mechanical property severely limits the practical device application. Given this, polycrystalline SnSe has been expected for improving mechanical properties, but the corresponding *ZT*s are much lower than those of the single crystals.[29-37] This is mainly because of the low oriented degree in polycrystalline samples, in other words, the poor texturing degree of polycrystalline SnSe leads to the low electrical conductivity. Many previous studies have shown that preferred orientation of polycrystalline SnSe grains is beneficial for improving the electronic transport properties.[38,39] The widely-used zone melting (ZM) is an efficient method to obtain good orientation, but the products still had poor mechanical properties.[40-41] Therefore, one need develop advanced textured sintering methods to prepare polycrystalline SnSe samples with good orientation and mechanical properties.

The liquid-phase sintering (LPS) method was successfully used to enhance the texturing degree and mechanical properties of layered TE materials, such as $Bi_{0.5}Sb_{1.5}Te_3$ and SnSe.[42,43] For example, the Na-doped SnSe polycrystalline samples were surrounded by the liquid phase of Te during the sintering process. The optimized orientation led to a greatly improved PF_{ave} of 6.01 μW $cm^{-1} K^{-2}$ and a higher ZT_{ave} of 0.45 between 300 and 830 K.[43] Besides, the hot deformation (HD) process was also applied to promote grain alignment and enhance texture modulation in Na-doped SnSe polycrystalline. Resulting from the increased μ_H by texturing in the HD process, a peak *ZT* value of 1.3 was achieved with a high PF of 10.2 μW $cm^{-1} K^{-2}$.[44] Obviously, both LPS and HD processes contribute to texture modulation and result in better electronic properties as well as mechanical properties in SnSe-based materials. Nevertheless, the HD procedure is some complicated and energy-consuming with poor repeatability,[44-48] while the LPS process may induce a higher thermal conductivity.[43,49-51]

Recently, the liquid-phase hot deformation (LPHD) technique was proposed in *n*-type $Bi_2(Te,Se)_3$ alloys.[52] This unconventional process combined the advantages of LPS and HD closely, generating the excellent TE properties. In this work, we used the LPHD method to prepare polycrystalline SnSe-

[a] College of Mechanics and Materials, Hohai University, Nanjing, 211100, China;
[b] Ningbo Institute of Materials Technology and Engineering, Chinese Academy of Sciences, Ningbo 315201, China;
[c] Normandie University, ENSICAEN, UNICAEN, CNRS, CRISMAT, Caen 14000, France;
†E-mail: tanxiaojian@nimte.ac.cn, huanghuajie@hhu.edu.cn, jjun@nimte.ac.cn.
Electronic Supplementary Information (ESI) available: [details of any supplementary information available should be included here]. See DOI: 10.1039/x0xx00000x

View Article Online
DOI: 10.1039/D0MA00405G

based materials. During the sintering process, the $Na_{0.03}Sn_{0.97}Se$ solid grains were initially surrounded by the liquid phase Te. Meanwhile, the prepared samples were gradually deformed in a larger graphite die with the extrusion of liquid phase Te. The grains recrystallization and orientation optimizing occurred by the plastic deformation. As a result, an enhanced carrier mobility μ_H and a reasonably reduced lattice thermal conductivity were realized for TE properties enhancement in the LPHD polycrystalline $Na_{0.03}Sn_{0.97}Se$ samples.

2. Experimental details

2.1 LPHD synthesis of polycrystalline $Na_{0.03}Sn_{0.97}Se$

Polycrystalline $Na_{0.03}Sn_{0.97}Se$ samples alloyed with different Te ratios (x = 0, 5 and 15 wt%) were prepared by melting high-purity raw materials in stoichiometric ratios (Sn granules, 5N; Se granules, 5N; Na chunk, 3N; Te chunk, 5N) in 10 mm vacuum-sealed quartz tubes (10^{-4} Torr). The mixtures were melted at 1193 K for 1h in the rocking furnace, ensuring composition homogeneity. The quartz tubes were then stayed upright and air-cooled, forming regular bulks. The obtained conical ingots were planished up and down to the cylinders (about 30 mm in height and 10 mm in diameter), and directly hot-deformed in larger ϕ16 mm graphite dies at 753 K under 60 MPa for 15 min parallel to the circular axis direction of the cylinder. Particularly, in order to ensure Te extrusion and HD occurring simultaneously, the ingots stayed at 725 K (melting point of Te) for 5min, and then pushed pressure slowly. Finally, the high-density LPHD samples of 8 mm in height and 16 mm in diameter were obtained.

2.2 Characterization

The phase structures and grain orientation were characterized by X-ray diffraction (XRD, Bruker D8, Germany), using Cu K_α radiation (λ=1.5406 Å). The chemical compositions and morphology were scanned by the energy dispersive spectroscopy (EDS, HKL MAX, Oxford Instruments) and scanning electron microscopy (SEM, Quanta FEG 250, FEI Co), respectively. The microstructures were investigated by using transmission electron microscopy (TEM, JEOL2100 HR).

2.3 Thermoelectric measurements

The electrical conductivity (σ) and Seebeck coefficient (α) were measured simultaneously using a ZEM-3 (Ulvac-Riko, Japan) from 300 to 830 K in a helium atmosphere. The thermal conductivity was determined by $\kappa = \rho C_P D$, where ρ is the sample density, C_p is the specific heat capacity, and D is the thermal diffusivity. The density ρ was measured using the Archimedes principle, the thermal diffusivity D was measured by the laser flash method (Netzsch, LFA-457, Germany), and the specific heat capacity C_p was obtained from previous reports.[27] Both the electronic and thermal transport properties were measured perpendicular to the pressure direction. The carrier concentration (n) and mobility (μ) were obtained from $n = 1/eR_H$ and $\mu = \sigma R_H$, where the Hall coefficient R_H was measured by a physical properties measurement system (Quantum Design, PPMS-9, US).

3. Results and discussion

3.1 XRD and morphology characterization

Fig. 1a shows the powder XRD patterns of the $Na_{0.03}Sn_{0.97}Se$-x%Te (x = 0, 5 and 15) polycrystalline samples at different prepared process, including the loose melted bulk before HP, the dense sintered bulks after LPHD, and the ejected materials during the LPHD process. Before HP, the main peaks of SnSe (JCPDS #48-1224) and elemental Te (JCPDS #36-1452) appeared. After HP, there were only peaks for the SnSe phase observed because that the elemental Te was "squeezed out" during the LPHD process. As shown in Fig. S1 of the Supporting Information, the extrudate in the x = 15 sample was more than that in the x = 5 sample. Consistent with previous reports,[42,43,49] the extrudate was also elemental Te as observed from the XRD results.

The XRD patterns for the bulk samples were measured on the surface perpendicular to the pressure direction as shown in Fig. 1b. All diffraction peaks can be indexed to the orthorhombic phase with a space group *Pnma* phase without obvious second phase detectable. It can be seen that the intensities of (400) and (111) reflection peaks were different among these samples, suggesting that the preferred orientation of LPHD samples seems to be parallel to the (400) plane. Moreover, the (400) peaks shifted toward lower angles with the increasing Te content, which probably results from that thimbleful Te atoms entered the Se sites and thereby increased the unit cell volume (see Fig. S2 of the Supporting Information).

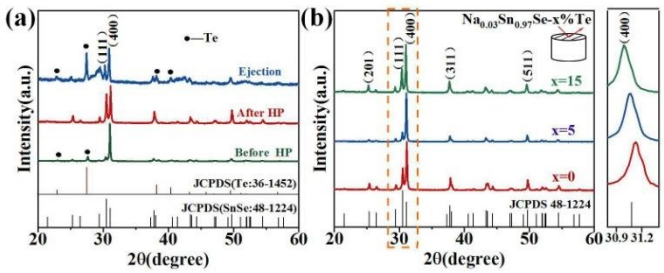

Fig. 1. (a) Powder XRD patterns for $Na_{0.03}Sn_{0.97}Se$-5%Te in different processes; (b) Bulk XRD patterns for $Na_{0.03}Sn_{0.97}Se$-x%Te (x = 0, 5 and 15) measured on the surface perpendicular to the pressing direction.

To evaluate the texture degree of $Na_{0.03}Sn_{0.97}Se$-x%Te LPHD samples, the orientation factor F of (hkl) plane was calculated using the Lotgering method by the following equations:

$$F = \frac{(P - P_0)}{(1 - P_0)} \quad (1)$$

$$P_0 = \frac{\sum I_0(00l)}{\sum I_0(hkl)}, P = \frac{\sum I(00l)}{\sum I(hkl)} \quad (2)$$

where $\sum I_0(hkl)$ and $\sum I(hkl)$ are the total of all relative intensities of (hkl) for randomly and preferentially oriented samples, respectively.[53] The high F value indicates high orientation degree of grains. As shown in Table 1, the orientation factor F(400) increases from 0.26 for the initial sample to 0.50 for the

View Article Online DOI: 10.1039/D0MA00405C

$Na_{0.03}Sn_{0.97}Se$-5%Te sample, indicating LPHD process enhance the texture for the compressed samples. However, with more element Te added to liquid-phase sintering, the *F*(400) value of the $Na_{0.03}Sn_{0.97}Se$-15%Te sample decreases to 0.32.

Table 1. The density ρ, relative density and orientation factor *F*(400) for the $Na_{0.03}Sn_{0.97}Se$-x%Te LPHD bulk samples.

Samples (x content)	ρ (g cm^{-3})	Relative density (%)	*F*(400)
x = 0	5.76	93.1	0.26
x = 5	6.03	97.5	0.50
x = 15	6.08	98.5	0.32

To further examine the textured structure, the SEM microscopic characterizations of $Na_{0.03}Sn_{0.97}Se$-x%Te (x = 0, 5 and 15) LPHD samples were presented in Fig. 2. The initial $Na_{0.03}Sn_{0.97}Se$ sample without Te addition exhibits disordered and less orientation, similar to most polycrystalline SnSe after HP process.[54,55] But the grains of the LPHD samples were refined and aligned in order, consistent with the enhanced orientation factor *F*(400) values.[41,43,44] On one hand, the liquid Te promotes the crystal plane slipping and preferred orientation during the sintering process. On the other hand, the hot deformation process boosts the grains inversion and recrystallization. Thus, the combined process of the LPHD technique can enhance the texture degree of SnSe-based material effectively. The grain size of LPHD samples increased significantly compared with the initial sample, especially the $Na_{0.03}Sn_{0.97}Se$-5%Te sample possessed the largest average grain size. Such a phenomenon was also observed in previous reports about SnSe and other layered TE materials,[56-58] and it was related to the electronic properties closely.

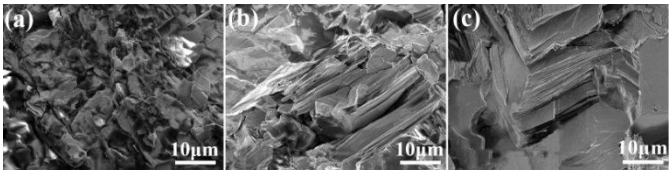

Fig. 2. The SEM image of the fractured surfaces parallel to the pressure direction for $Na_{0.03}Sn_{0.97}Se$-x%Te samples with (a) x= 0, (b) x= 5, and (c) x= 15.

Furthermore, the compositional homogeneity of the sample was confirmed by the back scattered electron image and EDS results were shown as Fig. S3 in Supporting Information. The results of $Na_{0.03}Sn_{0.97}Se$-15%Te indicated that the content of Na is much lower than the nominal one and the thimbleful Te is also observed in the lattice, consistent with above XRD results.

3.2 Electronic transport properties

The electronic transport properties of all samples perpendicular to pressing direction were summarized in Fig. 3. Fig. 3a shows the temperature dependent electrical conductivity σ of $Na_{0.03}Sn_{0.97}Se$ polycrystalline samples. For LPHD samples, σ firstly decreased with increasing temperature until ~670 K and then increased slightly, similar to the change tendency of the single crystal.[25,27] It can be seen that the LPHD technique significantly improved the σ of the $Na_{0.03}Sn_{0.97}Se$-x%Te samples near room temperatures. Especially for x = 5, the σ reached a maximum value of 218 S cm^{-1} at 303 K. Compared to the results of HD and LPS methods, the σ of LPHD sample increased by about 50% and 30% respectively.[43,44] Moreover, the LPHD samples exhibited excellent electrical properties during the whole temperature range. For example, the σ of $Na_{0.03}Sn_{0.97}Se$-5%Te sample at 810 K was 74 S cm^{-1}, which was still higher than those of other polycrystalline SnSe.[31,34,35,55]

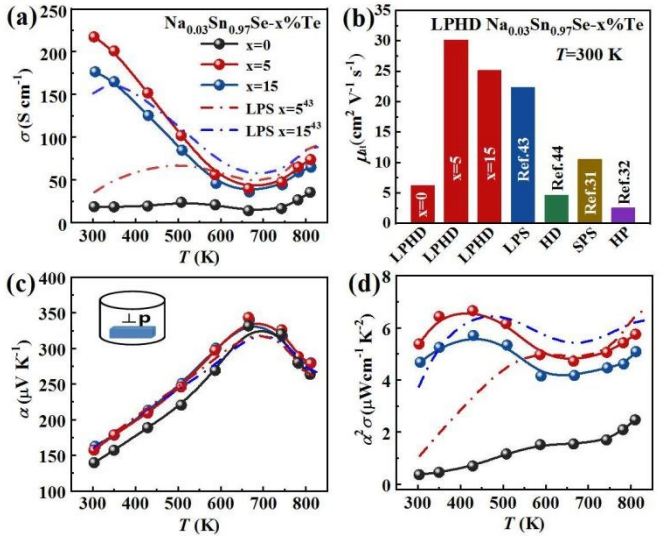

Fig. 3. Temperature dependence of $Na_{0.03}Sn_{0.97}Se$-x%Te (x = 0, 5 and 15) LPHD samples: (a) electrical conductivity, (b) room temperature Hall mobility with some previous reports as comparison, (c) Seebeck coefficient and (d) power factor.

Fig. 3b and Table 2 present the room temperature carrier concentration (*n*) and carrier mobility (μ_H) of LPHD samples. Similar to the results of previous HD and LPS samples,[43,44] the carrier concentrations of LPHD samples increased slightly and remained at a relatively stable level, mainly owing to the residual Te dopants that generated Sn vacancies.[59,60] More importantly, the room temperature carrier mobility improved significantly due to the enhancement of the texture degree. It can be seen that the carrier mobility increases obviously from 6.2 to 30.1 cm^2 V^{-1} s^{-1} of LPHD-5%Te, which is much higher than those of LPS[43] and HD samples.[44] The rapidly increased mobility was also observed in previous reports, and it may be owing to the barrier-like scattering originated from oxidation, defects or impurities at grain boundaries of SnSe materials.[61-63] The liquid Te may fill the grain gaps and thus reduce the oxidation and defects at the grain boundaries. Additionally, the stress induced by plastic deformation could be timely released by the extrusion of liquid Te during the HD process. As a result, the weakened grain boundary scattering by the LPHD process significantly improves the carrier mobility. Nevertheless, too much liquid Te (such as 15%Te) would wrap and lubricate the crystal grains, leading to less reduction of carrier mobility unexpectedly. As discussed above, the LPHD process enlarged the grain size and the corresponding texture degree was significantly raised (see the *F* values in Table 1), which were beneficial for the carrier mobility and electrical conductivity.

Table 2. The density (ρ), carrier concentration (n), Hall mobility (μ_H), and the Seebeck coefficient (α) at 300 K for polycrystalline $Na_{0.03}Sn_{0.97}Se$ samples prepared by different processes.

Methods	ρ (g cm^{-3})	n (10^{19} cm^{-3})	μ_H (cm^2 V^{-1} s^{-1})	α (μV K^{-1})
ZM	6.04	0.051	166	/
HD	5.72	2.67	4.7	198
LPS	6.03	3.16	22.3	145
LPHD-0%Te	5.76	1.89	6.2	139
LPHD-5%Te	6.03	4.51	30.1	158
LPHD-15%Te	6.08	4.39	25.1	163

Fig. 3c shows the temperature dependence of Seebeck coefficient (α). The relatively high α of all samples were positive, exhibiting *p*-type transport behavior. With the temperature increasing, the Seebeck coefficients first increased to the maximum and then decreased. The peak value was 327 μV K^{-1} at 680 K obtained in $Na_{0.03}Sn_{0.97}Se$-5%Te. Above 680 K, the reduction of α in all samples could be attributed to the thermal excitation of minority carriers (bipolar effect). Compared to the sample without Te addition, the α of $Na_{0.03}Sn_{0.97}Se$-x%Te increased obviously. It may be resulted from the suppressed the bipolar effect with improved carrier concentration.[43,52]

As shown in Fig. 3d, the LPHD samples exhibited much higher PF ($\alpha^2\sigma$) than the LPS one due to the significantly increased electrical conductivity. The maxima of $\alpha^2\sigma$ were found to be 6.65 μW cm^{-1} K^{-2} at 430 K and 5.75 μW cm^{-1} K^{-2} at 830 K for $Na_{0.03}Sn_{0.97}Se$-5%Te. It is worth noting that the PF value at room temperature is 5.38 μW cm^{-1} K^{-2}, which is the highest value observed in SnSe-based materials except SnSe single crystals. Due to the enhanced texture degree, the PF of all LPHD samples were maintained at higher values in the whole temperature range, particularly for $Na_{0.03}Sn_{0.97}Se$-5%Te. The average PF_{ave} of $Na_{0.03}Sn_{0.97}Se$-5%Te was 5.62 μW cm^{-1} K^{-2}, which was much higher than most *p*-type polycrystalline SnSe.[32,44,60,64] Such enhanced $\alpha^2\sigma$ was mainly attributed to the optimized texture degree and significantly improved electrical properties during the LPHD process.

3.3 Thermal conductivity and ZT value

Fig. 4a presents the total thermal conductivity κ of all samples as functions of temperature. The κ all gradually reduced as increasing temperature and then appeared an upturn around 743 K, arising from the *Pnma–Cmcm* phase transition. The LPHD samples, especially the $Na_{0.03}Sn_{0.97}Se$-5%Te one, exhibited lower κ than the one without excess Te in the whole temperature range. It is worthy to note that κ was significantly suppressed during the combined LPHD process as compared with the LPS method under the same condition.[43] The lowest κ value was 0.45 W m^{-1} K^{-1} at 743 K for the $Na_{0.03}Sn_{0.97}Se$-5%Te LPHD sample.

The electronic thermal conduction κ_e (see Fig. S4 of Supporting Information) is proportional to σ according to the Wiedemann-Franz law $\kappa_e = LT\sigma$, where the Lorenz number L was calculated by fitting of respective Seebeck coefficient values to the reduced chemical potential. Then the lattice thermal conduction κ_l was evaluated by $\kappa_l = \kappa - \kappa_e$. Fig. 4b presents the temperature dependent κ_l of the LPHD and previous LPS samples.[43] Much different from the previously reported LPS samples with Te addition, the κ_l of LPHD samples was obviously lower in the whole temperature range, which was mainly due to the introduced defects during the plastic deformation. As shown, the lowest κ_l value was obtained as 0.40 W m^{-1} K^{-1} in the x= 5 LPHD sample at 743 K.

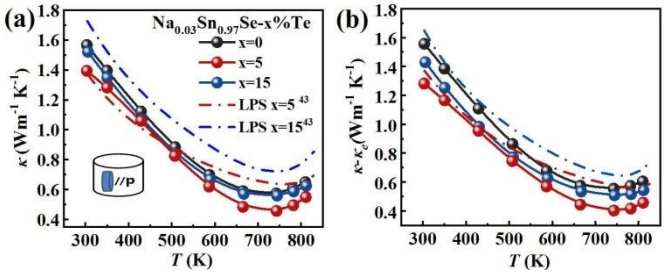

Fig. 4. Temperature dependences of (a) thermal conductivity; (b) lattice thermal conductivity. The data for LPS samples are plotted for comparison.[43]

To better understand the reduced κ_l of LPHD samples, TEM analyses were carried out on $Na_{0.03}Sn_{0.97}Se$-x%Te (x = 0, 5) samples. Mesoscale grains with size around 0.5 ~ 1 μm were observed in the sample as shown in Fig. 5a (x = 0) and 5b (x = 5). It can be clearly seen that the typical areas in Fig. 5b marked as 1 and 2 possess many strain-field domains, which were ascribed to dislocation effect in previous report.[65] The high-resolution TEM (HRTEM) image of region 1 in Fig. 5b was shown in Fig. 5c. Fig. 5d presents the inverse Fourier transformation (IFFT) picture along (400) plane reflections of the red box region in Fig. 5c, many dislocation defects could be readily observed. Moreover, interface regions with selenium precipitates and $SnSe_2$ second phase embedded in the matrix could be seem from the HRTEM images and EDS results shown

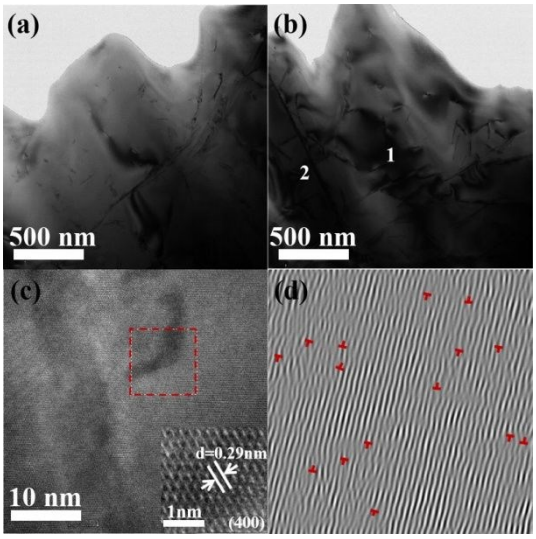

Fig. 5. Microstructure of the LPHD samples: (a) Low-magnification TEM image of $Na_{0.03}Sn_{0.97}Se$-0%Te; (b) Low-magnification TEM image of $Na_{0.03}Sn_{0.97}Se$-5%Te with the defects in the matrix; (c) HRTEM image from (b) region marked 1 with the FFT image and its interplanar spacing; (d) Inverse FFT image of the red box in panel (c) obtained from (400) reflection.

as Fig. S6 and Table S1 in the Supporting Information. These emerged phonon scattering centers during the LPHD process may strengthen the phonon scattering and decrease the κ_l. Additionally, similar to many previous LPS results of Bi_2Te_3 and

SnSe,[42,43,52] excess Te addition led to a slightly increased κ_l in $Na_{0.03}Sn_{0.97}Se$-x%Te samples, which needs further investigation in the future.

Fig. 6a displays the temperature dependence of *ZT* values for all samples. As shown, the *ZT*s were roughly increased with the increasing temperature. The maximum *ZT* value was 0.9 at 780 K for the $Na_{0.03}Sn_{0.97}Se$-5%Te sample. Since the PFs were limited at higher temperature, such peak *ZT* was not very competitive than previous reports.[19,20,36,44] However, comparing with the results of normal LPS or HD methods, a higher averaged *ZT* value (ZT_{ave}) was achieved by the LPHD technique as summarized in Fig. 6b. Between the temperature range of 300 to 810 K, our LPHD-prepared polycrystalline $Na_{0.03}Sn_{0.97}Se$ exhibited a ZT_{ave} of 0.49, which was obviously higher than previous reported $Na_{0.03}Sn_{0.97}Se$ polycrystalline.[31,32,43,44,60] The improved *ZT*s at lower temperature resulted from both the high carrier mobility in more textured structure and the obvious reduction of κ_l by the enhanced phonon scattering.

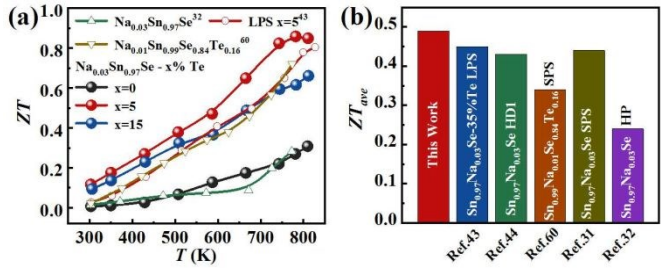

Fig. 6. (a) Temperature dependence of *ZT* for LPHD samples; (b) Average *ZT* values from 300 to 810 K for our $Na_{0.03}Sn_{0.97}Se$-5%Te LPHD sample and other previous reported polycrystalline $Na_{0.03}Sn_{0.97}Se$. [31,32,43,44,60]

Conclusions

In summary, the polycrystalline $Na_{0.03}Sn_{0.97}Se$-x%Te (x = 0, 5 and 15) samples were successfully prepared by a convenient and low-cost LPHD technique, which combined advantages of the LPS and HD processes. For the electronic transport, the texture of the sample was significantly enhanced and the grains showed a strong orientation along the (400) plane. The carrier mobility was effectively boosted, leading to higher electrical conductivity and power factor around room temperature. For the phonon transport, dense dislocation defects and $SnSe_2$ precipitates emerged during the LPHD process. These defects increased the phonon scattering rate and obviously reduced the lattice thermal conductivity. With these synergistical effects, a maximum *ZT* of 0.9 at 780 K and an average *ZT* value of 0.49 between 300 and 810 K were obtained in the $Na_{0.03}Sn_{0.97}Se$-5%Te LPHD materials. This work provides a novel technique for realizing high thermoelectric performance in SnSe-based materials through texture modification.

Conflicts of interest

There are no conflicts to declare.

Acknowledgements

View Article Online
DOI: 10.1039/D0MA00405G

This study was supported by the National Science Foundation of China (51872301 and 21875273), Natural Science Foundation of Zhejiang Province (LY18A040008), and the Youth Innovation Promotion Association of Chinese Academy of Sciences (2019298).

References

1. D. M. Rowe, Thermoelectric and Its Energy Harvesting, *CRC Press*, 2012.
2. L. E. Bell, Science, 2008, **321**, 1457-1461.
3. Y. Zheng, Y. Luo, C. Du, B. Zhu, Q. Liang, H. H. Hng, K. Hippalgaonkar, J. Xu and Q. Yan, *Mater. Chem. Front.*, 2017, **1**, 2457-2473.
4. A. Sorkina and S. Adams, *Mater. Adv.*, 2020, **1**, 184-196.
5. W. S. Liu and S. Q. Bai, *J. Materiomics*, 2019, **5**, 321-336.
6. G. J. Tan, L. D. Zhao and M. G. Kanatzidis, *Chem. Rev.*, 2016, **116**, 12123-12149.
7. W. Liu, H. S. Kim, Q. Jie and Z. Ren, *Sci. Mater.*, 2016, **112**, 3269-3274.
8. C. H. Lee, M. H. Ma, W. H. Li, P. C. Wei, Y. Y. Chen, Y. Zhao and J. W. Lynn, *Mater. Today Phys.*, 2019, **11**, 100171.
9. J. P. Heremans, V. Jovovic, E. S. Toberer, A. Saramat, K. Kurosaki, A. Charoenphakdee, S. Yamanaka and G. J. Snyder, *Science*, 2008, **321**, 554-557.
10. Y. X. Chen, Z. H. Ge, M. J. Yin, D. Feng, X. Q. Huang, W. Y. Zhao and J. Q. He, *Adv. Funct. Mater.*, 2016, **26**, 6836-6845.
11. Y. Pei, X. Shi, A. LaLonde, H. Wang, L. Chen and G. J. Snyder, *Nature*, 2011, **473**, 66-69.
12. X. J. Tan, H. X. Wang, G. Q. Liu, J. G. Noudem, H. Y. Hu, J. T. Xu, H. Z. Shao and J. Jiang, *Mater. Today*, 2018, **7**, 35-44.
13. L. S. Mao, Y. N. Yin, Q. Zhang, G. Q. Liu, H. X. Wang, Z. Guo, H. Y. Hu, Y. K. Xiao, X. J. Tan and J. Jiang, *Energy Environ. Sci.*, 2020, **13**, 616-621.
14. H. R. Yang, J. H. Bahk, T. Day, A. M. S. Mohammed, G. J. Snyder, A. Shakouri and Y. Wu, *Nano Lett.*, 2015, **15**, 1349-1355.
15. Z. Zhou, J. Yang, Q. Jiang, D. Zhang, J. Xin, X. Li, Y. Ren and X. He, *J. Am. Chem. Soc.*, 2017, **100**, 5723.
16. K. Biswas, J. He, I. D. Blum, C. I. Wu, T. P. Hogan, D. N. Seidman, V. P. Dravid and M. G. Kanatzidis, *Nature*, 2012, **489**, 414-418.
17. T. Zhu, Y. Liu, C. Fu, J. P. Heremans, J. G. Snyder and X. Zhao, *Adv. Mater.*, 2017, **29**, 1605884.
18. N. Neophytou, S. Foster, V. Vargiamidis, G. Pennelli and D. Narducci, *Mater. Today Phys.*, 2019, **11**, 100159.
19. Y. B. Luo, S. T. Cai, X. Hua, H. J. Chen, Q. H. Liang, C. F. Du, Y. Zheng, J. H. Shen, J. W. Xu, C. Wolverton, V. P. Dravid, Q. Y. Yan and M. G. Kanatzidis, *Adv. Energy Mater.*, 2018, **9**, 1803072.
20. M. M. Li, H. Z. Shao, J. T. Xu, Q. S. Wu, X. J. Tan, G. Q. Liu, M. Jin, H. Y. Hu, H. J. Huang, J. F. Zhang and J. Jiang, *J. Materiomics*, 2018, **4**, 321-328.
21. Z. Chen, B. Ge, W. Li, S. Lin, J. Shen, Y. Chang, R. Hanus, G. J. Snyder and Y. Pei, *Nat. Commun.*, 2017, **8**, 13828-13836.

22. Y. K. Xiao, G. X. Chen, H. M. Qin, M. L. Wu, Z. P. Xiao, J. Jiang, J. T. Xu, H. C. Jiang and G. J. Xu, *J. Mater. Chem. A*, 2014, **2**, 8512-8516.
23. R. Guo and S. Lee, *Mater. Today Phys.*, 2019, **12**, 100177.
24. C. W. Li, J. Hong, A. F. May, D. Bansal, S. Chi, T. Hong, G. Ehlers and O. Delaire, *Nat. Phys.*, 2015, **11**, 1063-1071.
25. K. L. Peng, X. Lu, H. Zhan, S. Hui, X. D. Tang, G. W. Wang, J. Y. Dai, C. Uher, G. Y. Wang and X. Y. Zhou, *Energy Environ. Sci.*, 2016, **9**, 454-460.
26. J. Hong and O. Delaire, *Mater. Today Phys.*, 2019, **10**, 100093.
27. L. D. Zhao, S. H. Lo, Y. Zhang, H. Sun, G. Tan, C. Uher, C. Wolverton, V. P. Dravid and M. G. Kanatzidis, *Nature*, 2014, **508**, 373-390.
28. C. Chang, M. Wu, D. He, Y. Pei, C.-F. Wu, X. Wu, H. Yu, F. Zhu, K. Wang, Y. Chen, L. Huang, J. F. Li, J. He and L. D. Zhao, *Science*, 2018, **360**, 778.
29. C. L. Chen, H. Wang, Y. Y. Chen, T. Day and G. J. Snyder, *J. Mater. Chem. A*, 2014, **2**, 11171-11176.
30. S. Li, Y. M. Wang, C. Chen, X. Li, W. Xue, X. Wang, Z. Zhang, F. Cao, J. Sui, X. Liu and Q. Zhang, *Adv. Sci.*, 2018, **5**, 1800598.
31. K. Peng, H. Wu, Y. C. Yan, L. J. Guo, G. Y. Wang, X. Lu and X. Y. Zhou, *J. Mater. Chem. A*, 2017, **5**, 14053-14060.
32. E. K. Chere, Q. Zhang, K. Dahal, F. Cao, J. Mao and Z. Ren, *J. Mater. Chem. A*, 2016, **4**, 1848-1854.
33. Y. H. Zhu, J. Carrete, Q. L. Meng, Z. W. Huang, N. Mingo, P. Jiang and X. H. Bao, *J. Mater. Chem. A*, 2018, **6**, 7959-7966.
34. N. K. Singh, S. Bathula, B. Gahtori, K. Tyagi, D. Haranath and A. Dhar, *J. Alloys Compd.*, 2016, **668**, 152-158.
35. D. B. Li, X. J. Tan, J. T. Xu, G. Q. Liu, M. Jin, H. Z. Shao, H. J. Huang, J. F. Zhang and J. Jiang, *RSC Adv.*, 2017, **7**, 17906-17912.
36. D. Li, J. C. Li, X. Y. Qin, J. Zhang, H. X. Xin, C. J. Song and L. Wang, *Energy*, 2016, **116**, 861-866.
37. F. Li, W. T. Wang, Z. H. Ge, Z. H. Zheng, J. T. Luo, P. Fan and B. Li, *Mater.*, 2018, **11**, 203-213.
38. Y. W. Li, F. Li, J. F. Dong, Z. H. Ge, F. Y. Kang, J. Q. He, H. D. Du, B. Li and J. F. Li, *J. Mater. Chem. C*, 2016, **4**, 2047-2055.
39. D. Feng, Z. H. Ge, D. Wu, Y. X. Chen, T. T. Wu, J. Li and J. Q. He, *Phys. Chem. Chem. Phys.*, 2016, **18**, 31821-31827.
40. X. Wang, J. T. Xu, G. Q. Liu, Y. J. Fu, Z. Liu, X. J. Tan, H. Z. Shao, H. C. Jiang, T. Y. Tan and J. Jiang, *Appl. Phys. Lett.*, 2016, **108**, 083902.
41. Y. J. Fu, J. T. Xu, G. Q. Liu, J. K. Yang, X. J. Tan, Z. Liu, H. M. Qin, H. Z. Shao, H. C. Jiang, B. Liang and J. Jiang, *J. Mater. Chem. C*, 2016, **4**, 1201-1207.
42. S. I. Kim, K. H. Lee, H. A. Mun, H. S. Kim, S. W. Hwang, J. W. Roh, D. J. Yang, W. H. Shin, X. S. Li, Y. H. Lee, G. J. Snyder and S. W. Kim, *Science*, 2015, **348**, 109-114.
43. J. H. Zhang, J. Xu, X. J. Tan, H. X. Wang, G. Q. Liu, H. Z. Shao, B. Yu, S. Yue and J. Jiang, *J. Mater. Chem. C*, 2019, **7**, 2653-2658.
44. S. J. Liang, J. T. Xu, J. G. Noudem, H. X. Wang, X. J. Tan, G. Q. Liu, H. Z. Shao, B. Yu, S. Yue and J. Jiang, *J. Mater. Chem. A*, 2018, **6**, 23730-23735.
45. L. P. Hu, H. J. Wu, T. J. Zhu, C. G. Fu, J. Q. He, P. J. Ying and X. B. Zhao, *Adv. Energy Mater.*, 2015, **5**, 1500411.
46. R. S. Zhai, L. P. Hu, H. J. Wu, Z. J. Xu, T. J. Zhu and X. B. Zhao, *ACS Appl. Mater. Interfaces*, 2017, **9**, 28577-28585.
47. C. Tan, X. J. Tan, B. Yu, G. Q. Liu, H. X. Wang, G. Q. Luo, J. T. Xu, Q. S. Wu, B. Liang and J. Jiang, *ACS Appl. Energy Mater.*, 2019, **2**, 6714-6719.
48. F. Li, R. S. Zhai, Y. H. Wu, Z. J. Xu, X. B. Zhao and T. J. Zhu, *J. Materiomics*, 2018, **4**, 208-214.
49. Y. Liu, Y. Zhang, S. Ortega, M. Ibanez, K. H. Lim, A. Grau-Carbonell, S. Marti-Sanchez, K. M. Ng, J. Arbiol, M. V. Kovalenko, D. Cadavid and A. Cabot, *Nano Lett.*, 2018, **18**, 2557-2563.
50. C. H. Zhang, M. D. L. Mata, Z. Li, F. J. Belarre, J. Arbiol, K. A. Khor, D. Poletti, B. B. Zhu, Q. Y. Yan and Q. H. Xiong, *Nano Energy*, 2016, **30**, 630-638.
51. R. Deng, X. Su, Z. Zheng, W. Liu, Y. Yan, Q. Zhang, V. P. Dravid, C. Uher, M. G. Kanatzidis and X. Tang, *Sci. Adv.*, 2018, **4**, eaar5606.
52. Y. H. Wu, Y. Yu, Q. Zhang, Ti. J. Zhu, R. S. Zhai and X. B. Zhao, *Advs. Sci.*, 2019, **6**, 1901702.
53. F. K. Lotgering, *J. Inorg. Nucl. Chem.*, 1960, **16**, 100-108.
54. T. R. Wei, G. Tan, X. Zhang, C. F. Wu, J. F. Li, V. P. Dravid, G. J. Snyder and M. G. Kanatzidis, *J. Am. Chem. Soc.*, 2016, **138**, 8875-8882.
55. Y. M. Han, J. Zhao, M. Zhou, X. X. Jiang, H. Q. Leng and L. F. Li, *J. Mater. Chem. A*, 2015, **3**, 4555-4559.
56. D. Kenfaui, D. Chateigner, M. Gomina and J. G. Noudem, *J. Alloys Compds.*, 2010, **490**, 472-479.
57. L. P. Hu, X. H. Liu, H. H. Xie, J. J. Shen, T. J. Zhu and X. B. Zhao, *Acta Materilia*, 2012, 60, 4431-4437.
58. H. Mun, K. H. Lee, S. J. Yoo, H. S. Kim, J. Jeong, S. H. Oh, G. J. Snyder, Y. H. Lee, Y. M. Kim and S. W. Kim, *Acta Materilia*, 2018, **159**, 266-275.
59. M. Hong, Z. G. Chen, L. Yang, T. C. Chasapis, S. D. Kang, Y. Zou, G. J. Auchterlonie, M. G. Kanatzidis, G. J. Snyder and J. Zou, *J. Mater. Chem. A*, 2017, **5**, 10713-10721.
60. T. R. Wei, C. F. Wu, X. Z. Zhang, Q. Tan, L. Sun, Y. Pan and J. F. Li, *Phys. Chem. Chem. Phys.*, 2015, **17**, 30102-30109.
61. Z. H. Ge, D. S. Song, X. Y. Chong, F. S. Zheng, L. Jin, X. Qian, L. Zheng, R. E. Dunin-Borkowski, P. Qin, J. Feng and L. D. Zhao, *J. Am. Chem. Soc.*, 2017, **139**, 9714-9720.
62. Y. K. Lee, K. Ahn, J. Cha, C. J. Zhou, H. S. Kim, G. Choi, S. I. Chae, J. H. Park, S. P. Cho, S. H. Park, Y. E. Sung, W. B. Lee, T. Hyeon and I. Chung, *J. Am. Chem. Soc.*, 2017, **139**, 10887-10896.
63. S. Wang, S. Hui, K. L. Peng, T. P. Bailey, X. Y. Zhou, X. F. Tang and C. Uher, *J. Mater. Chem. C*, 2017, **5**, 10191-10200.
64. S. S. Sassi, C. Candolfi, J. B. Vaney, V. Ohorodniichuk, P. Masschelein, A. Dauscher and B. Lenoir, *Appl. Phys. Lett.*, 2014, **104**, 212105.
65. D. Maier, *Solid State Commun.*, 2002, **122**, 565.